Insights into the roles of surface oxygen species of manganese oxides for the ozone elimination at ambient temperature

Lei Zhang[1], sheng wang[2], lirong Lv[3], Yang Ding[3], dongxu Tian[3], and Shudong Wang[3]

[1]Dalian Institute of Chemical Physics
[2]Dalian Institute of chemical physics
[3]Affiliation not available

May 7, 2020

Abstract

Manganese oxides with varied Mn valance states but identical morphology were synthesized. Their behaviors of ozone decomposition were investigated following the order of Mn3O4 < Mn2O3 < MnO2 < MnO2-H-200. It was deduced that the superior O3 decomposition capacity for MnO2-H-200 was strongly associated with abundant oxygen vacancies. Among Mn3O4, Mn2O3 and MnO2, the difference on O3 decomposition efficiency was dependent on divergent nature of oxygen vacancy. DFT calculation revealed that Mn3O4 and MnO2 possessed lower formation energy of oxygen vacancy, while MnO2 had the minimum desorption energy of peroxide species (O2*), suggesting that the promotion of the O3 decomposition capability was attributed to the easier O2* desorption. The insights on the deactivation mechanism for MnO2-H-200 further validated the assumptions. As the reaction proceeded, adsorbed oxygen species accumulated on the catalyst surface, and a portion of them were transformed to lattice oxygen.

Abstract

Manganese oxides with varied Mn valance states but identical morphology were synthesized via a facile thermal treatment of γ-MnOOH. And their behaviors of ozone decomposition were investigated following the order of $Mn_3O_4 < Mn_2O_3 < MnO_2 < MnO_2$-H-200. In combination with XRD, SEM, BET, TEM, H_2-TPR, O_2-TPD and XPS characterization, it was deduced that the superior O_3decomposition capacity for MnO_2-H-200 was strongly associated with abundant oxygen vacancies on its surface. Among Mn_3O_4, Mn_2O_3 and MnO_2, the difference on O_3 decomposition efficiency was dependent on divergent nature of oxygen vacancy. DFT calculation revealed that Mn_3O_4 and MnO_2 possessed lower formation energy of oxygen vacancy, while MnO_2 had the minimum desorption energy of peroxide species (O_2^*). It was deduced that the promotion of the O_3decomposition capability was attributed to the easier O_2^* desorption. The insights on the deactivation mechanism for MnO_2-H-200 further validated the assumptions. As the reaction proceeded, adsorbed oxygen species accumulated on the catalyst surface, and a portion of them were transformed to lattice oxygen. An irreversible generation of oxygen vacancy led to the deactivation of the catalyst.

Introduction

Ozone (O_3) as a typical secondary pollution is considered to be detrimental to human health and plant growth because of its strong oxidation capacity [1, 2]. It is generally recognized that the ground-level ozone is sourced from the photochemical reaction between volatile organic compounds (VOCs) and nitrogen oxides (NO_x) in the presence of heat and sunlight. Since the concentration of VOCs and NO_xhas been increasing with the increasing of the population density of the world, ozone pollution becomes more and serious [3]. Especially in some special circumstance, ozone hazards are more prominent such as in indoor environment and aircraft cabin [4]. Thus, the U.S. Environmental Protection Agency updated the National Ambient Air

Quality Standards for ground-level ozone from 75 ppb to 70 ppb [5]. Among the various routes known to eliminate ozone contamination, ozone catalytic decomposition has shown significant promise as an alternative way due to its efficiency and safety. Nevertheless there are a number of desirable characteristics for an ozone decomposition catalyst, among which superior activity and stability are crucial. Of course low cost is also a pursuit in view of application. Though precious metals own higher performance for ozone decomposition, transition metal oxides still are the optimum option in consideration of the scarcity of precious metals. Among transition metal oxides such as Co_3O_4, CeO_2, CuO and MnO_2 etc, MnO_2 is the most active oxide owing to multiple valence states [6]. As a result, numerous manganese oxides (MnO_x) with different Mn valences or particle morphologies have been reported with satisfactory catalytic performance for ozone elimination over the recent years [7, 8]. However, MnO_x is easily deactivated in the presence or absence of water vapor, so the reason why the catalyst deactivated is important for the rational design of the effective catalyst [9, 10].

Possible ozone decomposition mechanism over MnO_x catalyst was investigated by detecting the intermediate species. The peroxide species were identified by in situ Raman spectroscopy with isotopic labeling experiments by Oyama et al, and the reaction mechanism was elucidated as below [11, 12]:

O_3 + *- O* +O_2 (1)

O_3 + O*- O_2* + O_2 (2)

O_2* - O_2 + * (3)
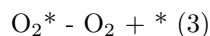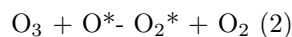
in which * represents the active sites, and O_2* stands for peroxide species. The primary reactions above are generally assumed to take place at oxygen vacancies with cations on the MnO_x surface, since oxygen vacancies can influence the O_3 and/or oxygen intermediates adsorption/desorption behaviors [10, 13-17]. Zhu et al showed that the adsorption energy of O_3 was increased when oxygen vacancies were generated into the α-MnO_2 lattice, indicating oxygen vacancies were more favorable for O_3 adsorption [15]. Gong et al [18] found that cubic Cu_2O exposed plane owned higher efficiency of O_3 decomposition and resistance to water vapor, which was ascribed to weakly adsorbed O_2* intermediate on the cubic Cu_2O. According to defect engineering, the adsorption strength of binding of adsorbed oxygen intermediates to the MnO_x surface depends on the property of oxygen vacancies, which is related to the elemental composition and structure of MnO_x [19, 20]. As the most efficient catalyst for O_3 decomposition, MnO_x was widely studied owing to its multiple oxidation states. Higher Mn^{3+} ratio on Mn/TiO_2 owned superior O_3 decomposition activity [21]. Similar result was obtained that manganese with lower oxidation states was favorable in decomposition of ozone [22, 23]. As indicated that the valence of Mn can significantly influence the ozone decomposition performance. Moreover, when Mn was coated on the support, the introduction of support will add the complexity between Mn valence and activity [24, 25]{Rakesh Radhakrishnan, 2001 #725}. Therefore, to avoid the effects of support, it is necessary that pure MnO_x should be synthesized to elucidate the intrinsic mechanism on O_3 decomposition. Even for the unsupported α-MnO_2, the α-MnO_2 nanofibers exhibited the best activity, which is ascribed to abundant oxygen vacancy on its preferentially exposed (211) facet [26]. So the effects of morphology should be further avoided.

In the study, MnO_2, Mn_2O_3 and Mn_3O_4 nanorods with identical morphologies were synthesized and oxygen vacancies were introduced to the surface of MnO_2-H-200 via hydrogen reduction. Their behaviors of ozone decomposition were studied. The dependence of their catalytic activity on the surface Mn valence was investigated. In combination with DFT calculation, the intrinsic mechanisms were also analyzed on O_3 catalytic decomposition.

2. Experimental section

2.1 Catalyst preparation

Firstly, γ-MnOOH nanorod was synthesized by a facile redox precipitation process. Then the corresponding β-MnO_2, α-Mn_2O_3 and Mn_3O_4 were prepared by calcining γ-MnOOH nanorods under different temperature and atmosphere. The details of preparation precedure and chemicals invloved are shown in Supporting information (SI).

2.2 Characterization

The crystalline structure of as-prepared samples was characterized by XRD. And their morphologies were observed by SEM and TEM. Texture properties were obtained by N_2-adsorption isotherms. And their redox capacities were tested by H_2-TPR and O_2/O_3-TPD. To further validate the oxygen mobility on the samples, XPS, FT-IR and Raman spectroscopies were also measured. The details of characterization are shown in Supporting information (SI).

2.3 Computational Methods

Density functional theory (DFT) calculations were carried out by the Vienna ab initio simulation package (VASP). The projector augmented wave (PAW) pseudo-potential was adopted to describe the ion-electron interactions, and the PW91 gradient-corrected functional was employed in the calculation of the exchange correlation energy. An energy cutoff of 400 eV was used for the plane-wave basis set. Numerical convergence thresholds of 10^{-6} eV in energy and 10^{-2} eV/Å in force were achieved on structural optimization. The Brillouin zone was sampled on the basis of the Monkhorst-Pack scheme with a $5\times5\times1$ k-point mesh [27]. A five-layer slab was used in the calculations. The atoms in the top two layers were fully relaxed while the rest of the atoms were fixed in their equilibrium positions.

Formation energy (E_f) of oxygen vacancy is defined as shown in the formula (4):

$$E_f = E_v - E_i - 1/2E_{O2} \quad (4)$$

E_v and E_i are total energy of the structure with and without an oxygen vacancy. E_{O2} is the total energy of an oxygen molecule.

The oxygen adsorption energy E_O was defined relative to the isolated substrate and the O_2 in the gas phase, as shown in the formula (5):

$$E_O = E_{[surf+O]} - E_{[surf]} - 1/2E_{O2} \quad (5)$$

where $E_{[surf + O]}$ and $E_{[surf]}$ are the total energies of the surface with and without the O adsorbate, respectively. E_{O2} is the total energy of an oxygen molecule.

2.4 Catalyst Activity Measurement

The activity of as-prepared samples for ozone decomposition was measured in a fixed bed continuous flow quartz reactor (6 mm i.d) using 0.1g of catalyst with size of 40-60 mesh at a temperature of 30°C. The total gas flowrate was 1000 mL/min with 500 mL/min air and 500 mL/min Ar, then the weight space velocity was 600,000 mL.h^{-1}.g^{-1}. Ozone was generated by the electrical stimulation of oxygen (OSAN, Dalian) and the inlet ozone concentration was 15 ppm. An ozone analyser (Model 49i, Thermo Scientific, USA) was used to detect the inlet and outlet ozone concentrations. The ozone conversion was calculated on the basis of inlet and outlet O_3 concentration (C) as follows:

$$O_3 \text{ conversion} = (C_{in} - C_{out})/C_{in} \times 100\% \quad (6)$$

3. Results and discussion

3.1 The crystal structures of the catalysts

The structure of the products by calcining the γ-MnOOH precursors (Figure S1) under different conditions was studied by XRD measurement. For clarity, the diffraction peak positions and the relative intensities of the standard patterns of MnO_2, Mn_2O_3, and Mn_3O_4 are also shown at the bottom of Figure 1. As can be seen from Figure 1, for the samples being calcined in air at 350°C, all the peaks of XRD patterns could be indexed to tetragonal β-MnO_2 (JCPDS card no. 72-1984). Further elevating temperature to 600°C, cubic α-Mn_2O_3 (JCPDS card no.71-0636) were obtained. Replacing the oxidative atmosphere to inert Ar, the obtained products consisted of tetragonal Mn_3O_4(JCPDS card no. 80-0382). After hydrogen reduction, the XRD patterns denoted as MnO_2-H-200 were in good agreement with β-MnO_2. However, the broad and

3

weak XRD features of MnO$_2$-H-200 indicated that β-MnO$_2$ owned a poor crystalline phase, which was led by introducing more defects during hydrogen reduction.
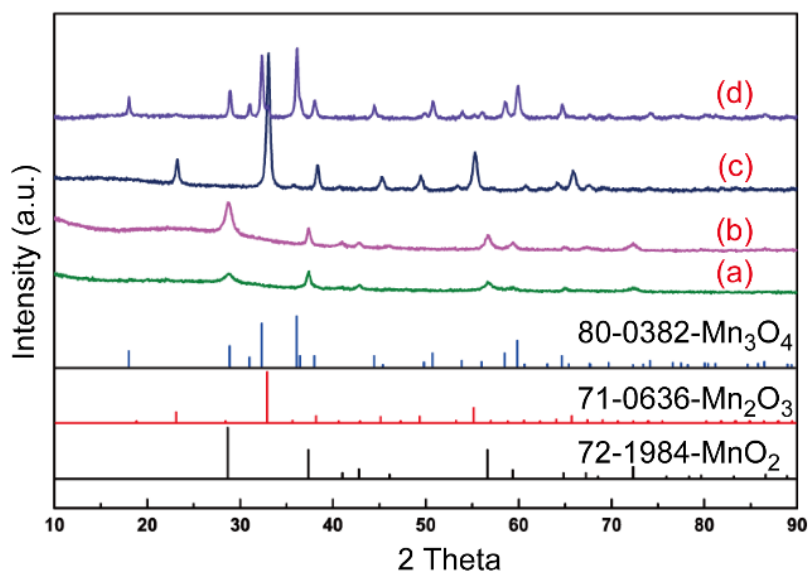

Figure 1. XRD patterns of the as-prepared products obtained by calcining the γ-MnOOH precursors under different conditions:(a) 350°C for 4h in air and then 200°C for 2h in H$_2$ (b) 350°C for 4h in air, (c) at 600°C for 2h in air, (d) 600°C for 4h in argon.

3.2 The morphology and microstructures of the catalysts

The morphologies of the as-obtained catalysts were investigated with SEM. Figure 2(a)-(d) showed the SEM images of MnO$_2$, Mn$_2$O$_3$, Mn$_3$O$_4$ and MnO$_2$-H-200, respectively. For all samples, it could be seen that the shape was dominated by one dimensional nanorods with a diameter of tens of nanometers and a length of several micrometers. To study the detailed structural features, the micro-morphologies of four samples were characterized by TEM. Figure 3(b) showed that MnO$_2$possessed the inter-planar distance of 0.31nm, corresponding to the (110) plane of β-MnO$_2$, which is in good agreement with the results of the selected-area electron diffraction (SAED). The MnO$_2$ had excellent crystallinity and displayed oriented growth along the [001] direction, and mainly exposed (110) facets. As shown in Figure 3(d) and (f), Mn$_2$O$_3$and Mn$_3$O$_4$ preferentially exposed (211) and (200) facets, respectively. For MnO$_2$-H-200, the lattice fringe image became more indiscernible than MnO$_2$(Figure 3(h)). The indistinct lattice fringe image of MnO$_2$-H-200 suggested that defects were generated due to oxygen element escaping from the MnO$_2$ lattice under H$_2$/Ar atmosphere.

4
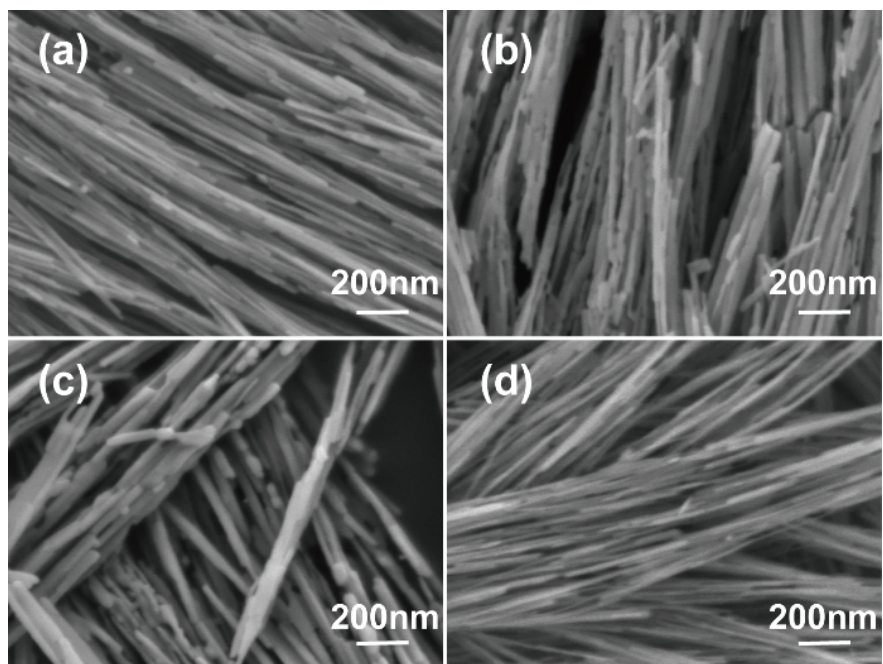
Figure 2. SEM images of MnOx catalysts: (a) MnO_2, (b) Mn_2O_3, (c) Mn_3O_4, (d) MnO_2-H-200.

(b) 0.31nm 0.31nm (1 1 0) (2 0 0) (1 -1 0) 10 nm

(c) 50 nm

8
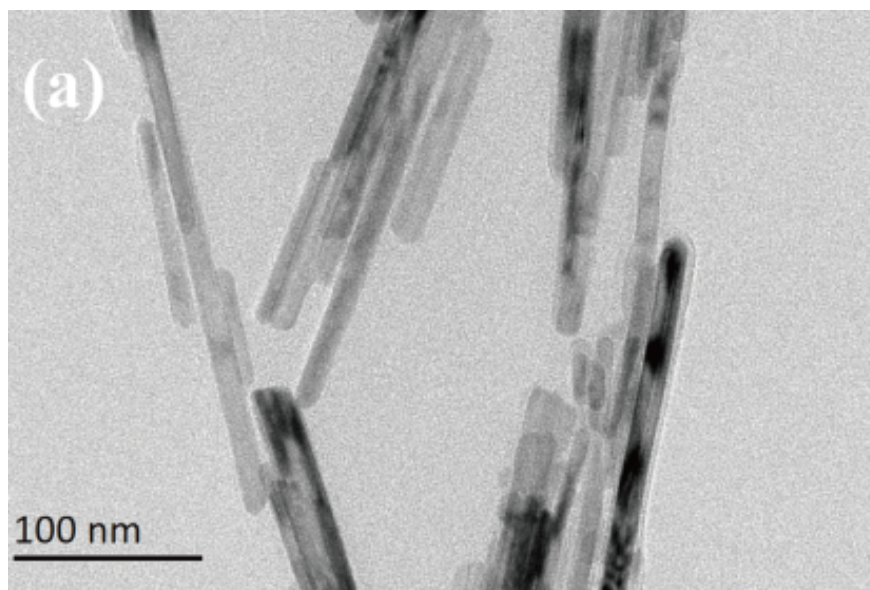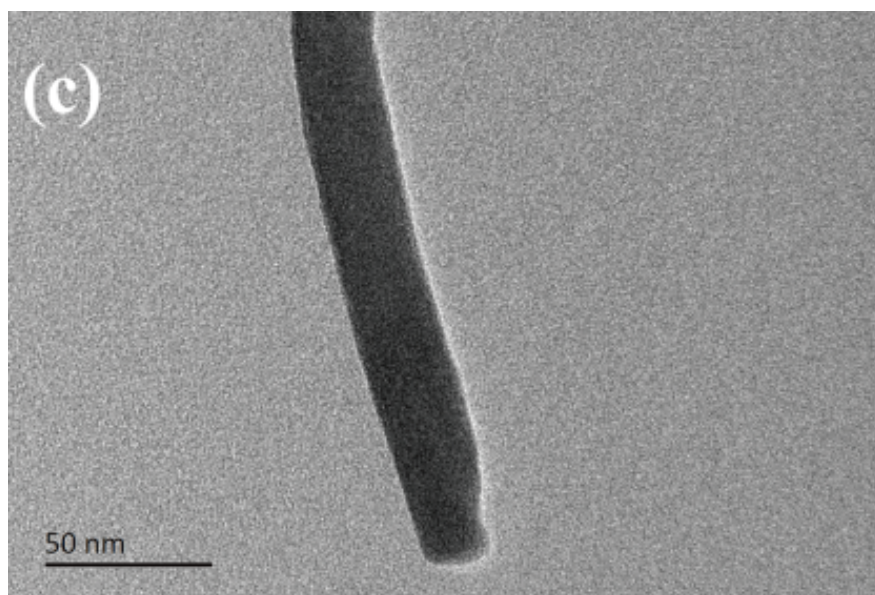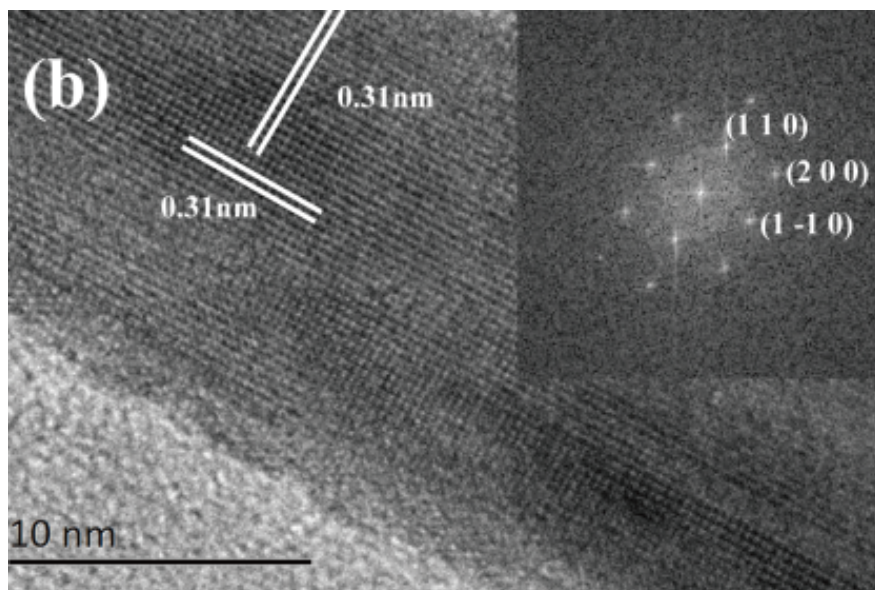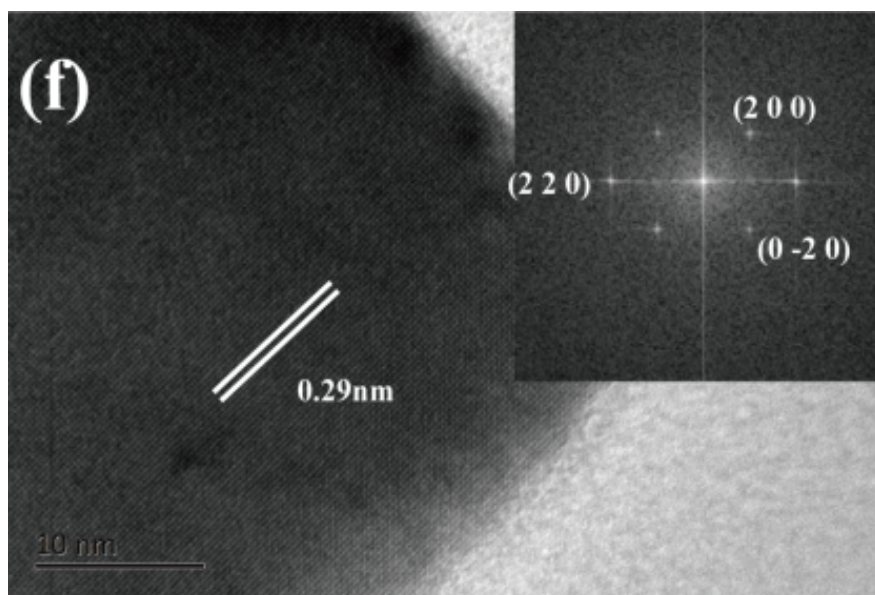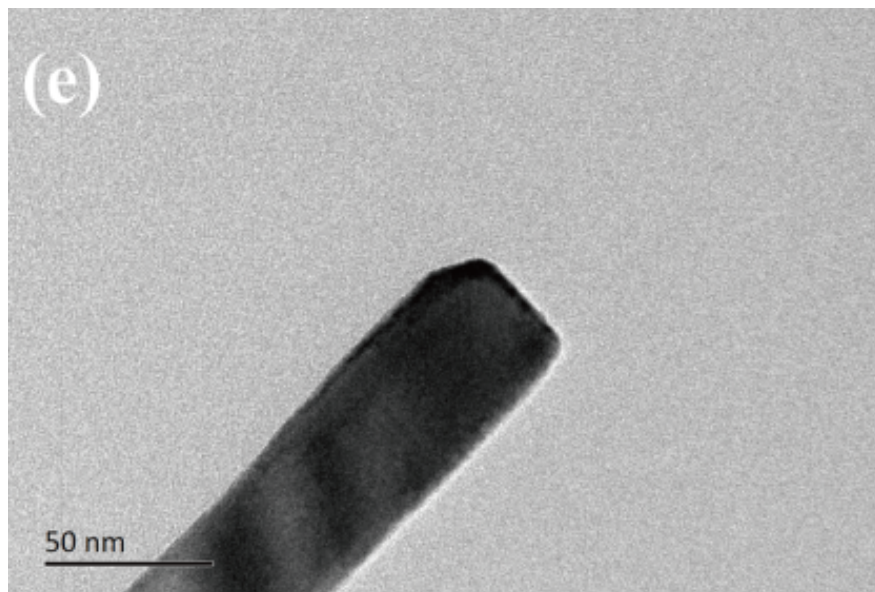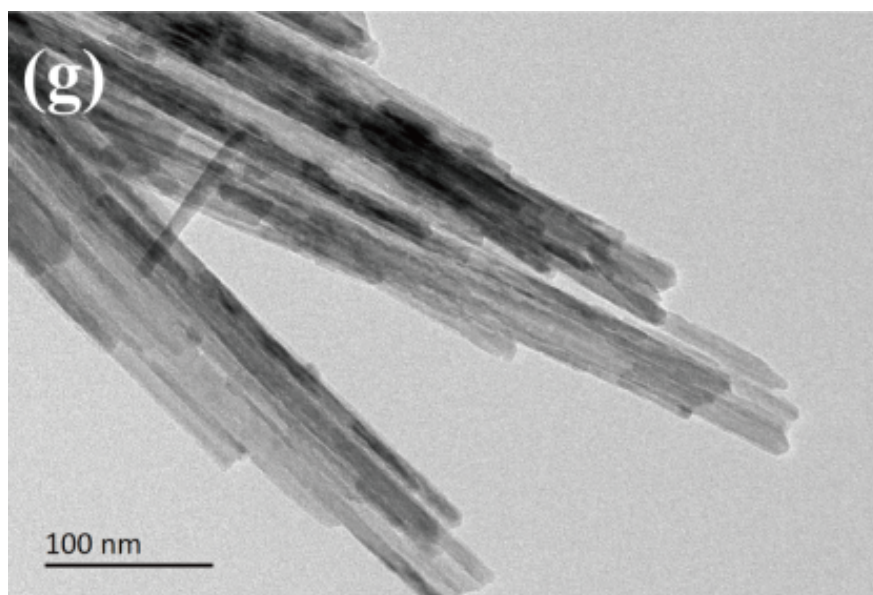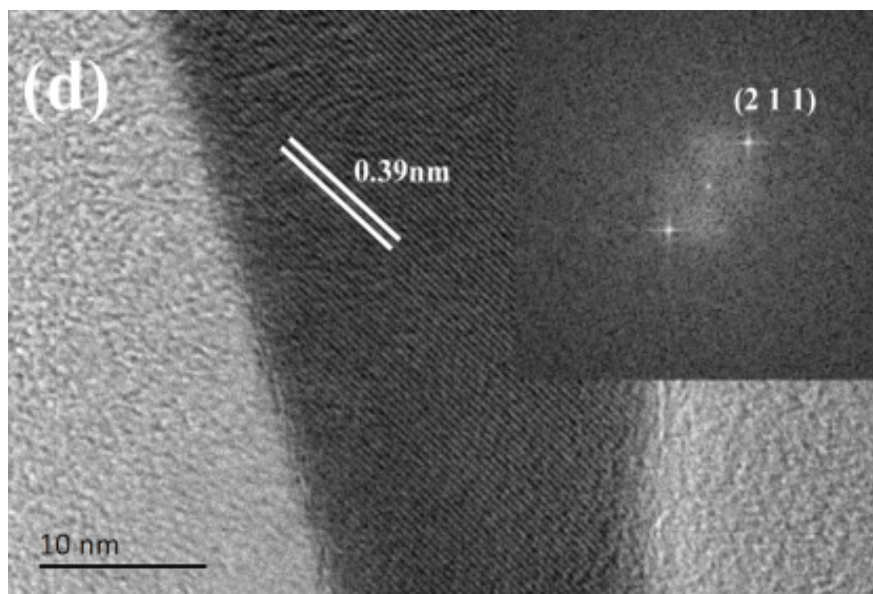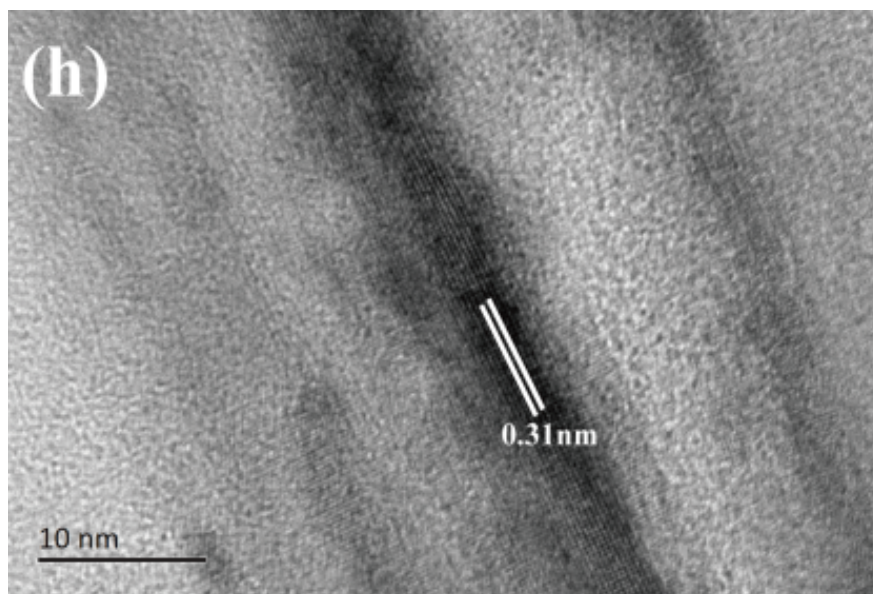
Figure 3. TEM images (with the SAED pattern inset) of MnO_x catalysts: (a,b) MnO_2, (c,d) Mn_2O_3, (e,f) Mn_3O_4, (g,h) MnO_2-H-200.

3.3 The redox property of the catalysts

The reducibility of the MnO_x above has been evaluated by H_2-TPR experiments and the results are shown in Figure 4. All the samples got green after H_2-TPR experiments. It indicated the samples were reduced into MnO. Only one reduction peak occurred for Mn_3O_4, which was attributed to the reduction of Mn_3O_4 to MnO. While two peaks were detected over other samples. The lower-temperature peak was ascribed to the reduction of MnO_2/Mn_2O_3 to Mn_3O_4, and the higher-temperature peak is attributed to the further reduction of Mn_3O_4 to MnO [28, 29]. Moreover, it should be noted that the low reduction temperature decreased from 306°C to 295°C for MnO_2 and MnO_2-H-200. Generally, low onset reduction temperature corresponds to better reducibility. As shown in Figure 4, the reducibility lied in the following sequence: $Mn_3O_4 < Mn_2O_3 < MnO_2 < MnO_2$-H-200, implied that abundant oxygen vacancies or high Mn valence can enhance reducibility of MnO_x catalyst.
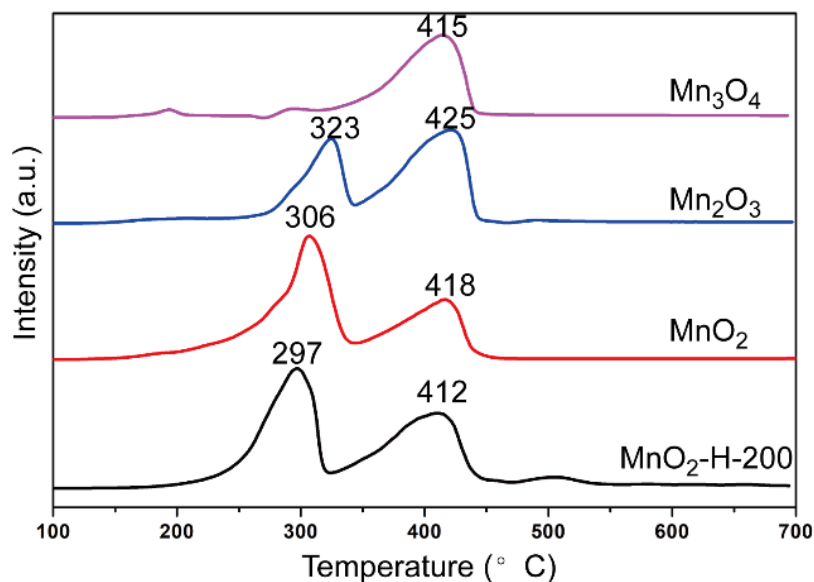
Figure 4. H_2-TPR profiles of MnO_x catalysts (MnO_2-H-200, MnO_2, Mn_2O_3 and Mn_3O_4

The type and mobility of oxygen species were determined by O_2-TPD and the results were shown in Figure 5. Generally, the O_2-TPD profile of MnO_2could be divided into three evolution peaks including low temperature($<350°C$), medium temperature($350-600°C$) and high temperature ($>600°C$) [30]. For the above MnO_x, the major peak centered at 519°C was ascribed to the transformation of MnO_2 to Mn_2O_3 due to the release of lattice oxygen. The high temperature peak ($>800°C$) was attributed to the successive transformation to Mn_3O_4. As shown in Figure 5, the oxygen desorption behaviors on manganese oxides at different valences were obviously different. Usually, the lower the desorption temperature of oxygen is, the looser it is bound to Mn within the MnO_xlattice. Therefore, MnO_2 and MnO_2-H-200 had higher oxygen mobility. The peak at below 200°C was sourced from the desorption of physically adsorbed O_2 [31]. As shown in the inset of Figure 5, the peak area of physically adsorbed O_2 is remarkably larger than that of other samples, indicating that more active sites were provided on MnO_2-H-200. For MnO_2-H-200, a new peak at 270°C was assigned as the release of surface lattice oxygen and chemisorbed oxygen located at surface vacancies, indicating that hydrogen reduction enhance the mobility of oxygen species at low temperature, which was important for the ozone elimination activity.

10
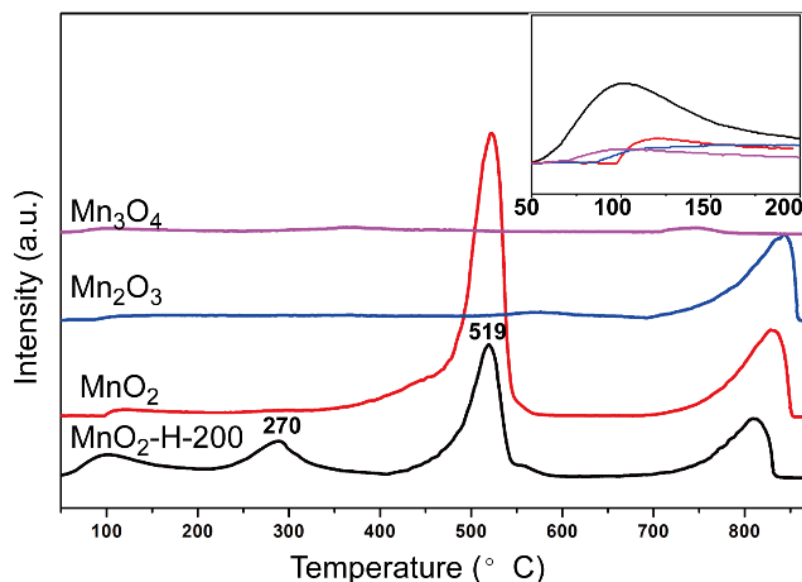
Figure 5 . O_2-TPD profiles of MnO_x catalysts (MnO_2-H-200, MnO_2, Mn_2O_3 and Mn_3O_4), inset with the large view of the profiles at the temperature range of 50-200°C

3.4 The characteristics of oxygen vacancies

The surface Mn state and oxygen species were investigated by XPS. The magnitude of Mn3s multiplet splitting could be used to calculate the average oxidation state(AOS) of Mn, according to the following relationship [32]:

AOS=8.956-1.126ΔE_S (7)

Where $[?]E_s$ is the binding energy difference between the doublet Mn3s peaks shown in Figure 6a.The results were summarized in Table 1. The calculated AOSs of MnO_2, Mn_2O_3 and Mn_3O_4 were lower than their theoretical values owing of surface oxygen defects. Moreover, the AOS of MnO_2-H-200 decreased to 3.22 from 3.78 of MnO_2 suggesting that the density of oxygen vacancy was enhanced via hydrogen reduction.

For the above MnO_x, the O1s spectrum shown in Figure 6b could be deconvoluted into two peaks to gain information on the nature of oxygen species. The one with lower binding energy at 529.5-530.2eV was assigned as the lattice oxygen (denoted as O_{latt}), and the other with higher binding energy at 531.3-531.4eV was ascribed as the surface-adsorbed oxygen (denoted as O_{ads}). Generally oxygen molecules were adsorbed at the oxygen vacancies of an oxide material [33]. And the ratio of O_{ads}/O_{latt} was an efficient parameter to characterize the relative abundance of oxygen vacancy in MnO_x. The more oxygen species adsorbed on the MnO_x surface, the higher oxygen vacancy density was. As was shown in Table 1, there were no remarkable differences on the ratios of O_{ads}/O_{latt} for MnO_2, Mn_2O_3 and Mn_3O_4. While MnO_2-H-200 exhibited the higher value of O_{ads}/O_{latt}ratio than those of MnO_2, Mn_2O_3 and Mn_3O_4, indicating that MnO_2-H-200 owned the most abundant surface adsorbed oxygen species, which was consistent with the results revealed by O_2-TPD.

11
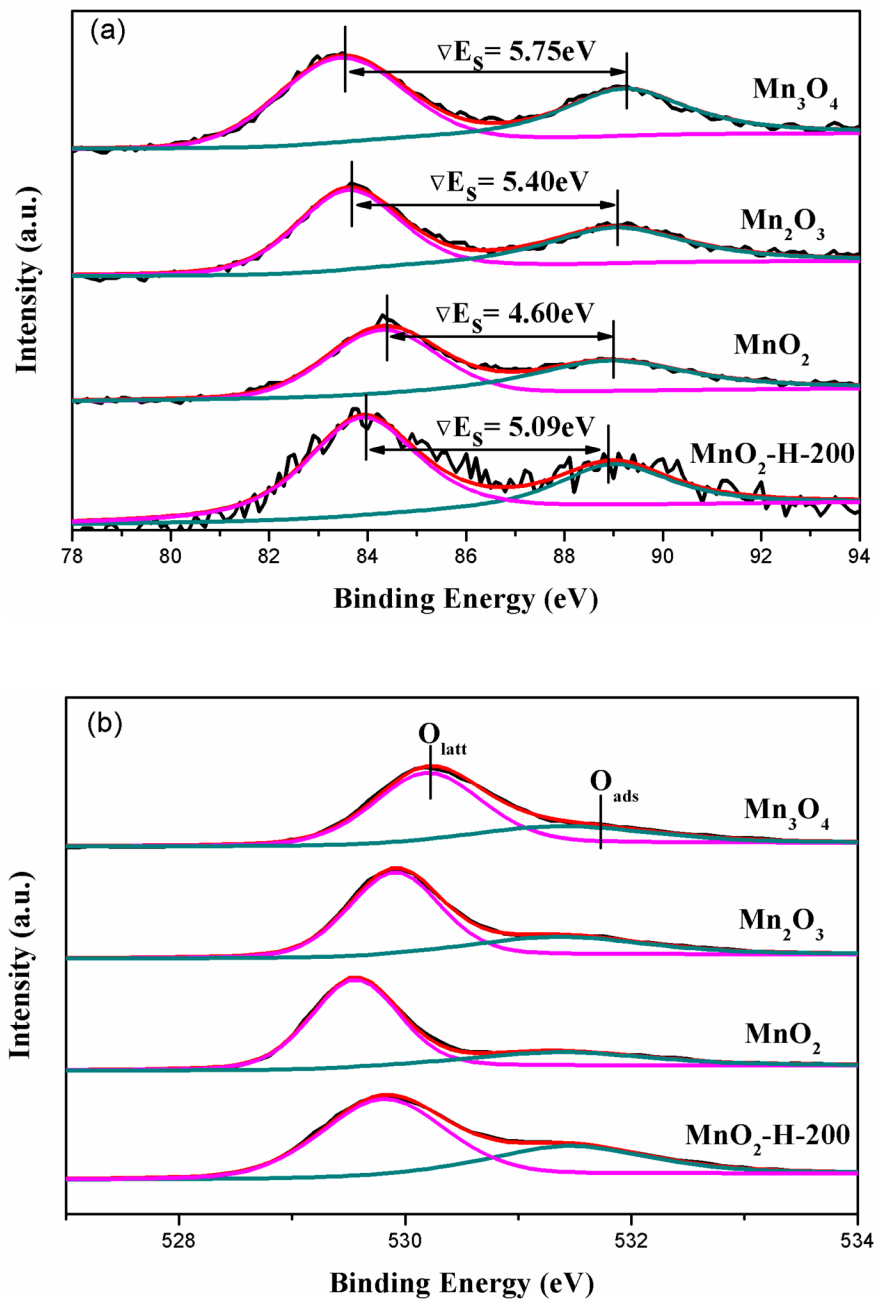
Figure 6 . (a)Mn 3s and (b) O1s XPS spectra of MnO_x catalysts (MnO_2-H-200, MnO_2, Mn_2O_3 and Mn_3O_4)

Table 1. XPS results of MnO_x catalysts (MnO_2-H-200, MnO_2, Mn_2O_3 and Mn_3O_4)

Catalysts	Mn3s AOS of Mn	O1s binding energy (eV)	O1s binding energy (eV)	Relatively intensity O_{ads} / O_{latt}
		O_{latt}	O_{ads}	
Mn_3O_4	2.48(8/3)	530.2	531.3	0.26
Mn_2O_3	2.88(3)	529.9	531.3	0.29

12

Catalysts	Mn3s AOS of Mn	O1s binding energy (eV)	O1s binding energy (eV)	Relatively intensity O_{ads} / O_{latt}
MnO_2	3.78(4)	529.5	531.3	0.27
MnO_2-H-200	3.22(4)	529.8	531.4	0.55

3.5 Catalytic activities on ozone decomposition

The catalytic activities of as-prepared MnO_x catalysts for ozone decomposition were evaluated at 30°C. As shown in Figure 7, the ozone conversion of all the MnO_x decreased with reaction time. Nevertheless MnO_2-H_2-200 showed a better stability, and its ozone conversion kept above 96% after 12h of reaction. While the conversion dropped to 87% for MnO_2, 43% for Mn_2O_3 and 12% for Mn_3O_4, respectively. MnO_2-H_2-200 showed the best performance of ozone decomposition due to the abundant surface oxygen vacancies revealed by O_2-TPD and XPS analysis.
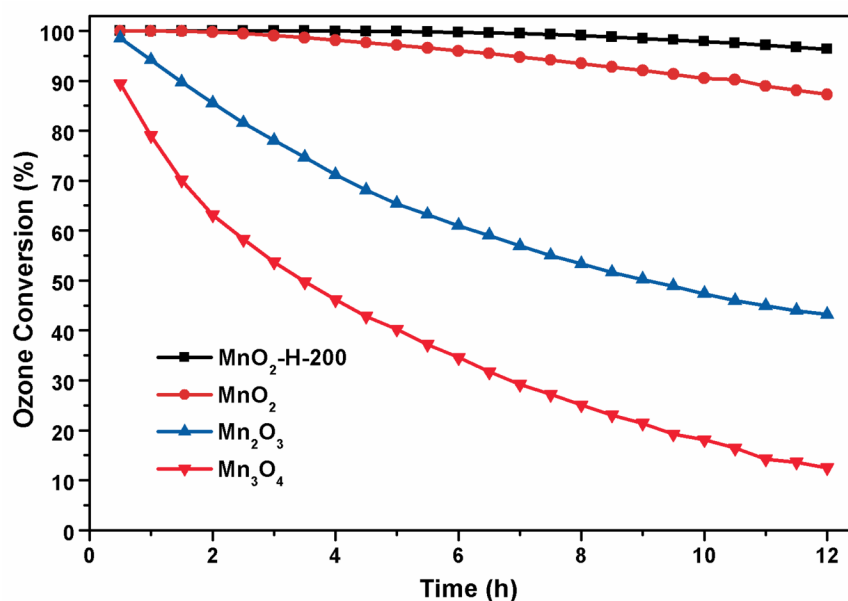
Figure 7 . Ozone conversion over different MnO_x catalysts (MnO_2-H-200, MnO_2, Mn_2O_3 and Mn_3O_4)

MnO_2, Mn_2O_3 and Mn_3O_4 showed distinctly different performance on ozone decomposition, although they had almost the same O_{ads}/O_{latt} ratio. As it is recognized that the improvement in catalytic performance may be due to higher surface area, BET surface area were obtained for the catalysts as shown in Table 2 and Figure S2. To exclude the influence from surface area, specific surface reaction rates of different MnO_x were shown in Table 2, in the following order: $MnO_2 > Mn_2O_3 > Mn_3O_4$. It indicated that their catalytic performances of O_3 decomposition were not likely dependent on their surface area among MnO_2, Mn_2O_3 and Mn_3O_4. The related study reported that the desorption of peroxide species O_2^* was the rate-limiting step during ozone catalytic decomposition. And the desorption procedure is a reduction process, in which electrons were transferred to the manganese center by O_2^* to form O_2. That is to say, the easier MnO_x reduces, the better the catalytic activity is. XPS results showed that the O1s binding energy of O_{latt} decreased in the following order: $MnO_2(529.5eV) < Mn_2O_3(529.9eV) < Mn_3O_4(530.2eV)$, suggesting that MnO_2 had the most loosely bound of Mn-O or the highest mobility of oxygen, which was consistent with the results of H_2-TPR and O_2-TPD. Since the three catalysts had comparable O_{ads}/O_{latt} ratio values, the nature of oxygen vacancies may play a crucial role in the desorption of O_2^*. However the gap on the nature of oxygen defects still needed to be elucidated by DFT calculation.

13

Table 2. Reaction rate after 3h time-on-stream test

| Catalysts	Specific surface area m^2g^{-1}	Reaction rate μmol g^{-1} h^1	Specific surface reaction rate μmol m^{-2} h^{-1}
Mn_3O_4	34.8	48.2	1.38
Mn_2O_3	43.8	172.8	3.94
MnO_2	54.4	349.5	6.42
MnO_2 -H-200	66.0	385.7	5.84

3.6 DFT calculations

The first-principle calculation was carried out using VASP program to further understand the formation of the oxygen vacancy and its effect on ozone decomposition. Based on the TEM images (Figure 3), the MnO_x selectively exposed different favorable facets. On three types of facets, including MnO_2 (110), Mn_3O_4 (200) and Mn_2O_3 (211), the deoxidation kinetics were studied. Top, bridge and hollow oxygen vacancy sites were all examined for each facet (Figure S3-S5). Formation energy (E_f) of oxygen vacancy was theoretically studied to reveal the energy of removal of lattice oxygen, as shown in Table 3. The process of oxygen vacancy formation often played a key role in catalytic activity, as for it was generally accepted as the active sites for ozone adsorption [34]. And literatures [9, 17] reported that the oxygen vacancy easier to be formed led to more active sites, resulting in a higher performance for ozone removal. In comparison with the oxygen vacancy formation energy, it can be drawn that the oxygen vacancy is difficult to form on Mn_2O_3(211) surface, owing to the relatively higher formation energy. It could be explained by the different coordination number of oxygen to manganese atoms.

The process that the O_2^* transforms into oxygen molecule can be viewed as oxygen desorption, so oxygen adsorption energy (E_o) on oxygen vacancy has been widely adopted as a descriptor for ozone elimination activity. The adsorption energy of O_2 on different kinds of oxygen vacancies on MnO_2 and Mn_3O_4 was also calculated and the results were shown in Table 3. Generally, a large E_o leads to the difficulty of the removal of O_2^*, thus catalytic activity was lowered. Compared to Mn_3O_4(200), MnO_2(110) was favorable for adsorbed O_2^* to desorb from the oxygen vacancy sites. A three-step sequence mechanism was reasonable to describe ozone decomposition on manganese oxides, (i) dissociative adsorption of ozone to form an O_2 molecule and an atomic O, with low energy barrier of 6 kJ/mol, (ii) reaction of the atomic O with gaseous ozone to form a peroxide species and an O_2 molecule, and (iii) desorption of O_2 to restore oxygen vacancy. The step (iii) is proved to be the rate-limiting step. Comparing with the oxygen adsorption energy, MnO_2(110) was favorable for the regeneration of the oxygen vacancies, enhancing the O_3 elimination capability, as shown in Figure 8. It is in good agreement with the experimental results.

Table 3. Formation energy (E_f) and oxygen adsorption energy (E_o) of different kinds of oxygen vacancies

		MnO_2 (110)	Mn_2O_3 (211)	Mn_3O_4 (200)
Formation energy (E_f) (eV)	Top	/	6.1197	/
	Bridge	2.9918	4.0208	2.0503
	Hollow	2.6895	5.1112	/
Oxygen adsorption energy (E_o) (eV)	Bridge	-2,5564	/	-4.3003
	Hollow	-2.3758	/	/

14
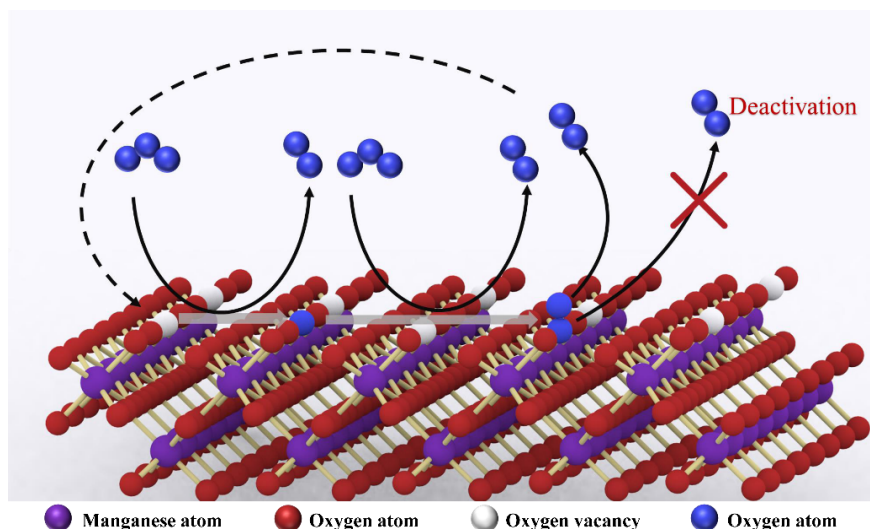
Figure 8 . Schematic illustration of O_3decomposition on MnO_2.

3.7 Mechanism of deactivation of ozone decomposition

Since the catalytic performance decreased with the reaction time for all MnO_x, it is necessary to investigate the catalyst deactivation mechanism to develop more efficient catalyst. The physiochemical performances for MnO_2-H-200 before and after reaction were studied. The catalysts, its ozone conversion dropping to 60% and 20%, were denoted as MnO_2-H-200-0.6 and MnO_2-H-200-0.2, respectively. The surface composition of the catalysts was investigated using XPS (Figure 9). The Mn AOS increased after reaction, accompanied with the binding energy of Mn2p shifting to higher energies, suggesting a higher Mn AOS for deactivated catalysts. And the peak intensity for surface adsorbed oxygen (O_{ads}) increased with the decline of ozone conversion, implying that the oxygen intermediates accumulated on the catalyst surface during the reactions. The intermediates occurring on the partially deactivated catalysts were characterized by FT-IR (Figure S6). The results indicated that a new peak at 1380cm^{-1} occurred, which was assigned to oxygen species derived from peroxide species O_2^* [35, 36]. Combined with XPS results, it was speculated that the irreversible O_2^* desorption on oxygen vacancies led to the accumulation of intermediate oxygen species, resulting in the deactivation of MnO_2-H-200.

16
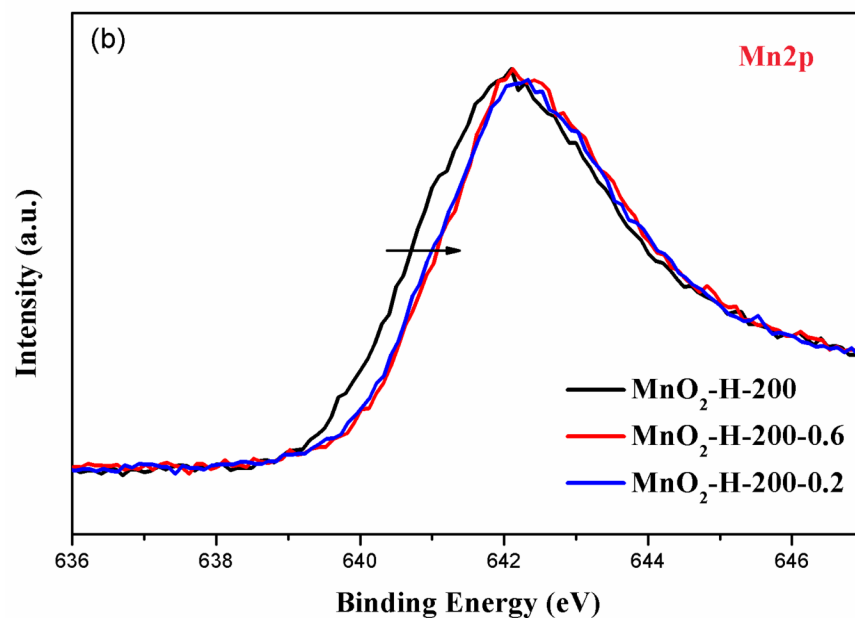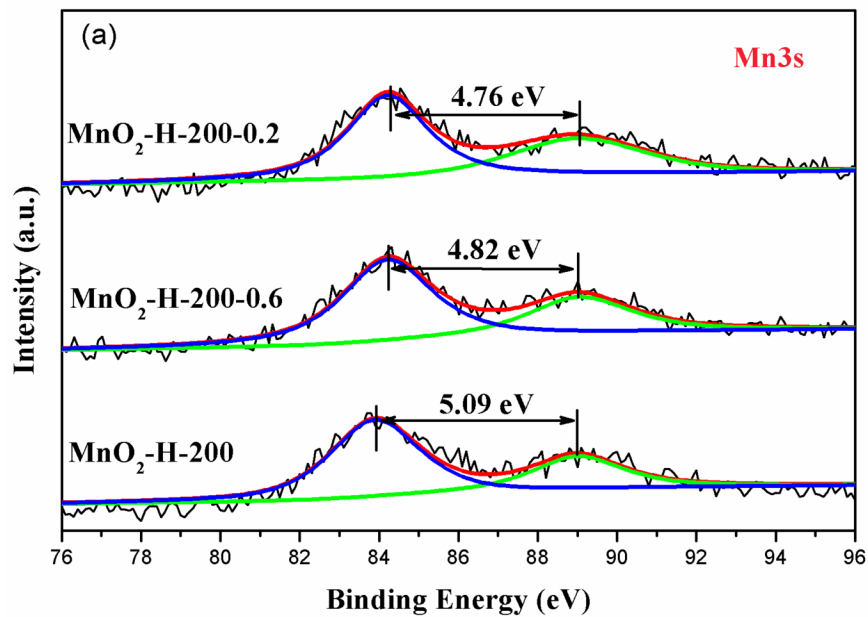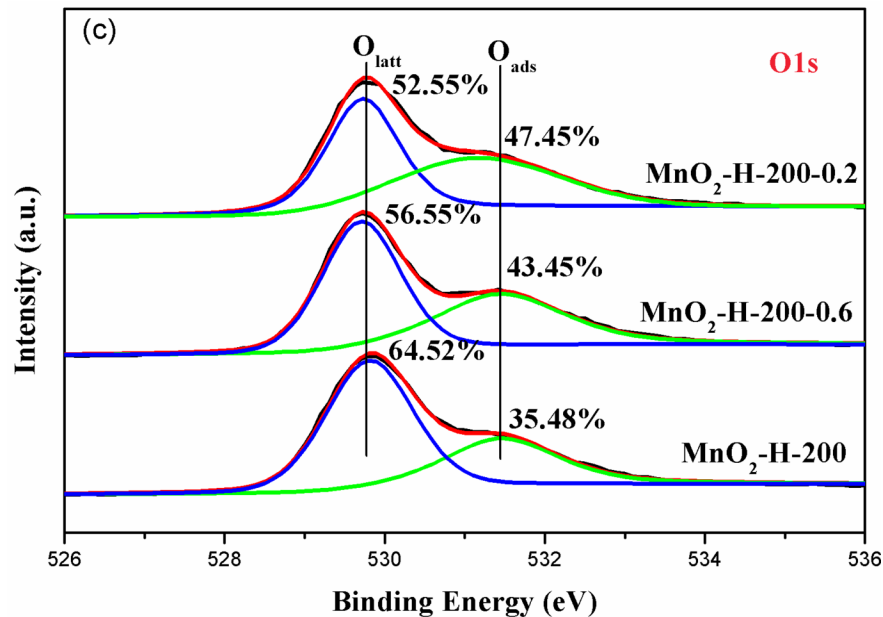
Figure 9 . (a) Mn 3s, (b) Mn 2p$_{3/2}$ and (c) O1s XPS spectra of MnO$_2$-H-200 at different ozone conversion (1, 0.6 and 0.2)

To further verify the irreversible O$_2^*$ desorption on MnO$_2$-H-200, O$_2$-TPD was conducted and was shown in Figure 10. The O$_2$-TPD profile in lower temperature range was deconvoluted into several peaks (Figure 10b). According to previous studies, the desorption peaks of O$_2^*$ and O* located at less than 200°C and in the range of 200-350°C, respectively. The O$_2^*$ was regarded as the intermediate of ozone decomposition. The desorption temperature of the peaks attributed to O$_2^*$ followed the order: MnO$_2$-H-200-0.2 >MnO$_2$-H-200-0.6 >MnO$_2$-H-200, suggesting that O$_2^*$ species were relatively stable on the spent catalysts. As the desorption of O$_2^*$ is the rate-limiting step for ozone decomposition, the difficult desorption of O$_2^*$ on the catalyst hindered the recovery of the oxygen vacancies. As a result, it caused a decrease of active sites and a low ozone conversion. The results indicated though the O$_2^*$ desorption process was relatively reversible for MnO$_2$-H-200, the residual O$_2^*$ difficult to desorb from the surface of the catalyst might hinder the subsequent cycles, hence decreasing its active sites with time.
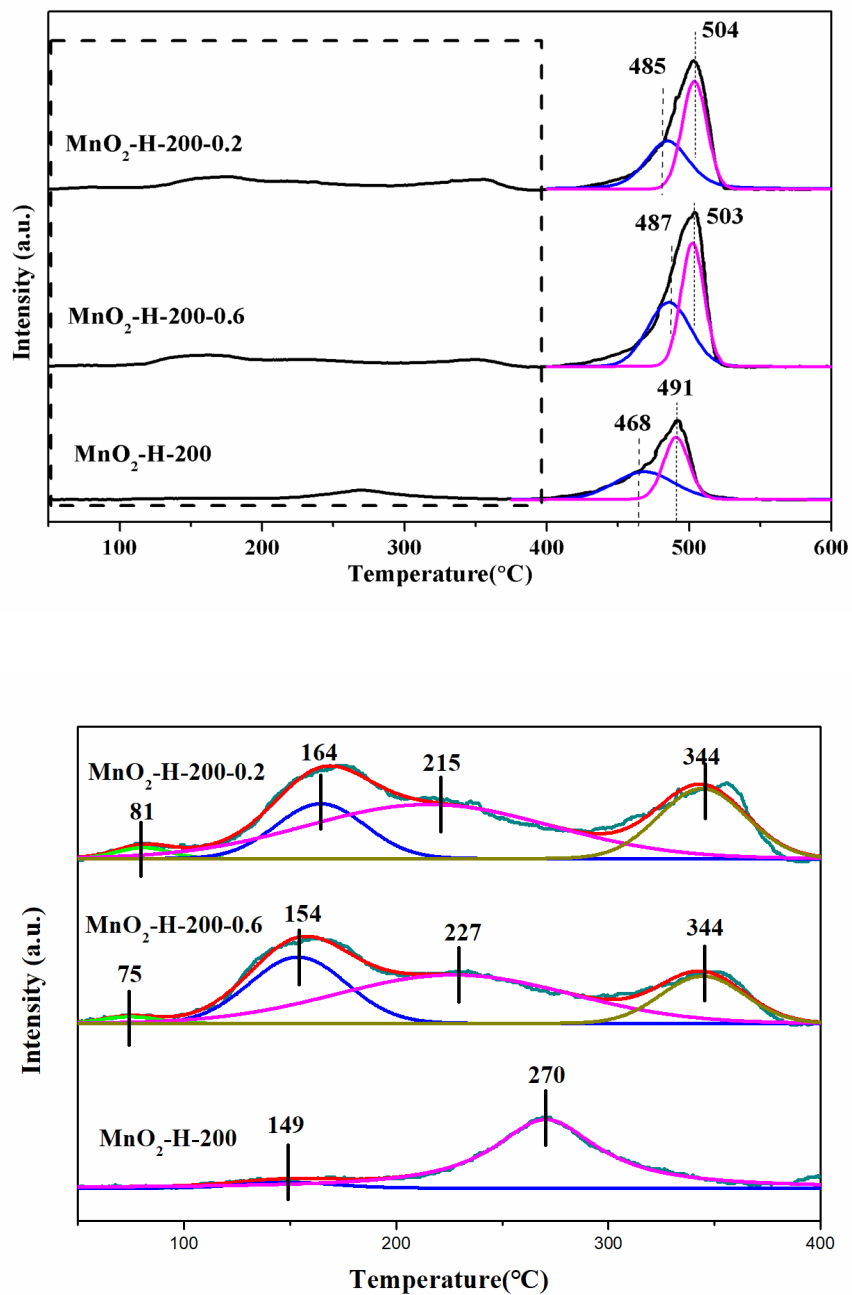
Figure 10 . O_2-TPD profile of MnO_2-H-200 at different ozone conversion (1, 0.6 and 0.2): (a) the temperature range of 50-600°C and (b) the peak-peak fitting at the temperature range of 50-400°C

For MnO_2-H-200, two desorption peaks occurring at 468°C and 491°C were attributed to the gradual escapes of the lattice oxygen close to the surface and the bulk oxygen species, respectively. They both shifted to higher temperature for the spent catalysts, which indicated that oxygen mobility got weakened and the strong Mn-O bond was formed in the octahedral MnO_6 framework. The consistent results were obtained in H_2-TPR (Figure 11). Generally, when oxygen vacancies were introduced to MnO_2, the formation of Mn^{3+} could result in the Jahn-Teller distortion and thus facilitate to weaken Mn-O bond. So the lower oxygen mobility of the used catalysts might be caused by the unrecovered oxygen vacancies.

18
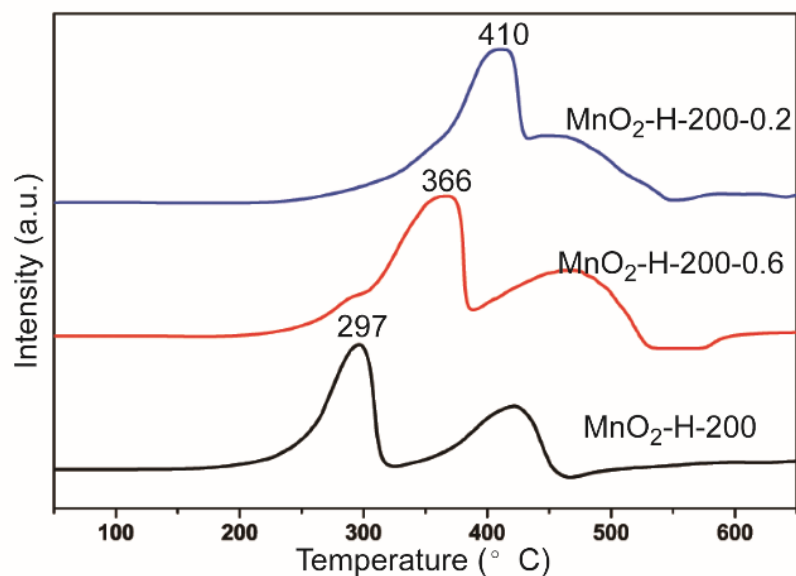
Figure 11 . H$_2$-TPR profile of MnO$_2$-H-200 at different ozone conversion (1, 0.6 and 0.2)

In order to further confirm the influence of the accumulation of O$_2$* on the catalysts, the structures of MnO$_2$-H-200 before and after reaction were analyzed by XRD as shown in Figure 12. The diffraction peaks of the reacted catalysts corresponded well to the standard PDF card (JCPDS 72-1984) of MnO$_2$ and no extra impurities were observed, which indicated that the accumulation of O$_2$* had slight effect on the catalyst crystal structure or the changes were too trivial to detect.
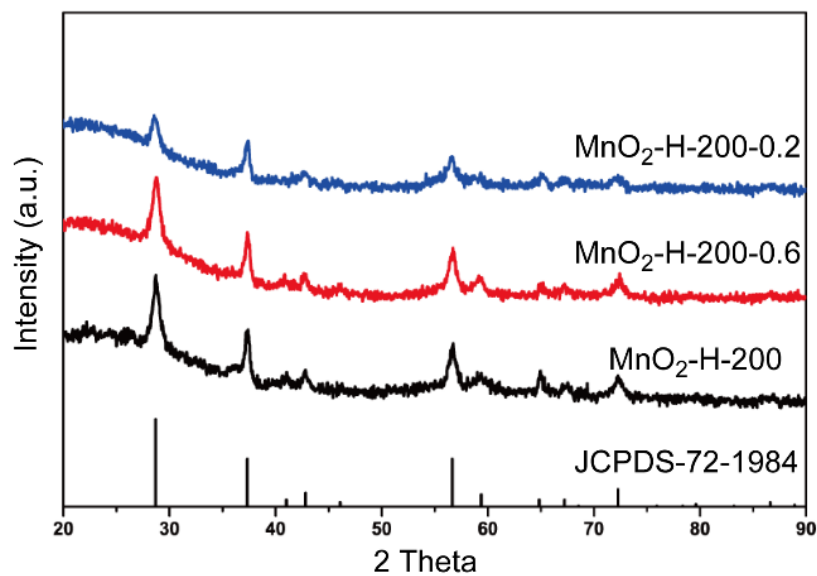
Figure 12 . XRD patterns of MnO$_2$-H-200 at different ozone conversion (1, 0.6 and 0.2)

Further evidence on the micro-structural transformation during deactivation was obtained by Raman spectra

(Figure 13), which can afford abundant information on short-range structure. For MnO$_2$-H-200, its characteristic peaks were centered at 533 and 665 cm^{-1}, which were attributed to the stretching mode of the Mn-O bond in MnO$_6$ octahedra in β-MnO$_2$. While a new peak at 574cm^{-1}appeared on the spectra of the reacted catalysts, which was indicative of the stretching vibrations of MnO$_6$ octahedra with an interstitial space consisting of (1×2) channels [37-40]. It reflected a formation of γ-MnO$_2$ structure for the reacted catalysts, suggesting that the adsorbed intermediate oxygen species transformed into lattice oxygen. It was further elucidated that the irreversible desorption on MnO$_2$-H-200 led to the loss of active sites and a decay of ozone conversion.
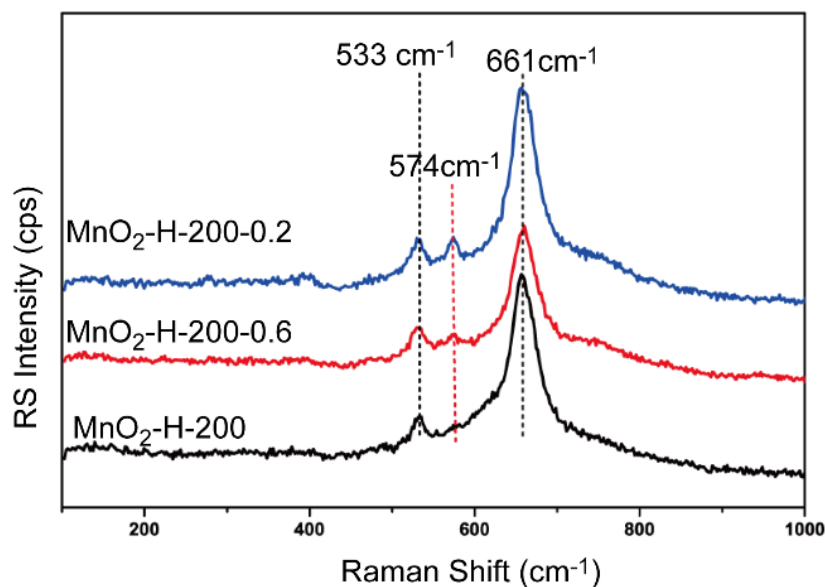
Figure 13 . Raman spectra of MnO$_2$-H-200 at different ozone conversion (1, 0.6 and 0.2)

4. Conclusions

A series of MnO$_x$ catalysts (MnO$_2$, Mn$_2$O$_3$ and Mn$_3$O$_4$) with different Mn valences were synthesized by calcining γ-MnOOH through tuning the calcination temperature and atmosphere. MnO$_2$-H-200 was obtained by reducing MnO$_2$ using hydrogen. The catalytic activity of the above MnO$_x$ towards ozone decomposition followed the order of MnO$_2$-H-200 >MnO$_2$> Mn$_2$O$_3$> Mn$_3$O$_4$.MnO$_2$ showed better activity than Mn$_2$O$_3$ and Mn$_3$O$_4$ due to its lower formation energy of oxygen vacancy and desorption energy of peroxide species. Especially among three catalysts, the least desorption energy of peroxide species on MnO$_2$ facilitated to the occurrence of rate-limiting reaction step. The surface oxygen vacancy got enriched for MnO$_2$-H-200 by H$_2$-reduction. The results elucidated that both the nature and abundance of oxygen vacancies have a decisive influence on the catalytic decomposition of ozone. Take an example of MnO$_2$-H-200, the insights on deactivation mechanism further validated that the catalytic stability of O$_3$ decomposition was strongly associated with the regeneration capacity of oxygen vacancy. The transformation from adsorbed oxygen species to lattice oxygen led to an irreversible generation of oxygen vacancy, which changed the property of the surface of the catalysts and resulted in the difficult desorption of O$_2$*. Hence it caused the deactivation of the catalyst.

Declaration of Competing Interest

The authors declare no competing financial interest.

20

Appendix A. Supplementary data

The following is Supplementary data to this article:

Catalyst preparation; Catalyst characterization; XRD patterns of the as-prepared γ-MnOOH; N_2 adsorption and desorption isotherms of the different MnO_x catalysts; Top plane view and the oxygen vacancy sites of the preferentially exposed crystal plane for various MnOx during DFT calculation; FT-IR spectra of MnO_2-H-200 and partially deactivate MnO_2-H-200 catalysts.

References

[1] R.K. Saari, Y. Mei, E. Monier, F. Garcia-Menendez, Effect of Health-Related Uncertainty and Natural Variability on Health Impacts and Cobenefits of Climate Policy, Environmental science & technology, 53 (2019) 1098-1108.

[2] Z. Chen, L. Yang, Y. Huang, P. Spencer, W. Zheng, Y. Zhou, S. Jiang, W. Ye, Y. Zheng, W. Qu, Carcinogenic risk of N-Nitrosamines in Shanghai Drinking Water: Indications for the Use of Ozone Pretreatment, Environmental science & technology, 53 (2019) 7007-7018.

[3] J.H. Xiao Lu, Lin Zhang,Owen R. Cooper,Martin G. Schultz, Xiaobin Xu,, M.G. Tao Wang, Yuanhong Zhao, and Yuanhang Zhang, Severe Surface Ozone Pollution in China A Global Perspective, Environmental Science & Technology Letters, 5 (2018) 487-494.

[4] C. Weisel, C.J. Weschler, K. Mohan, J. Vallarino, J.D. Spengler, Ozone and ozone byproducts in the cabins of commercial aircraft, Environmental science & technology, 47 (2013) 4711-4717.

[5] C.J. Weschler, Ozone in Indoor Environments: Concentration and Chemistry, Indoor Air, (2000) 269-288.

[6] B. Dhandapani, S.T. Oyama, Gas phase ozone decomposition catalysts, Applied Catalysis B: Environmental, 11 (1997) 129-166.

[7] Y. Liu, P. Zhang, J. Zhan, L. Liu, Heat treatment of $MnCO_3$: An easy way to obtain efficient and stable MnO_2 for humid O_3decomposition, Applied Surface Science, 463 (2019) 374-385.

[8] M. Wang, P. Zhang, J. Li, C. Jiang, The effects of Mn loading on the structure and ozone decomposition activity of MnO_x supported on activated carbon, Chinese Journal of Catalysis, 35 (2014) 335-341.

[9] G. Zhu, J. Zhu, W. Li, W. Yao, R. Zong, Y. Zhu, Q. Zhang, Tuning the K(+) Concentration in the Tunnels of alpha-MnO_2 To Increase the Content of Oxygen Vacancy for Ozone Elimination, Environmental science & technology, 52 (2018) 8684-8692.

[10] J. Jia, P. Zhang, L. Chen, Catalytic decomposition of gaseous ozone over manganese dioxides with different crystal structures, Applied Catalysis B: Environmental, 189 (2016) 210-218.

[11] Wei Li, G.V.Gibbs, S.T. Oyama, Mechanism of Ozone Decomposition on a Manganese Oxide Catalyst. 1. In Situ Raman Spectroscopy and Ab Initio Molecular Orbital Calculations, Journal of American Chemical Society, 120 (1998) 9041-9046.

[12] Wei Li, G.V.Gibbs, S.T. Oyama, Mechanism of Ozone Decomposition on a Manganese Oxide Catalyst. 2. Steady-State and Transient Kinetic Studies, Journal of American Chemical Society, 120 (1998) 9047-9052.

[13] C. Wang, J. Ma, F. Liu, H. He, R. Zhang, The Effects of Mn^{2+} Precursors on the Structure and Ozone Decomposition Activity of Cryptomelane-Type Manganese Oxide (OMS-2) Catalysts, The Journal of Physical Chemistry C, 119 (2015) 23119-23126.

[14] Y. Liu, P. Zhang, Catalytic decomposition of gaseous ozone over todorokite-type manganese dioxides at room temperature: Effects of cerium modification, Applied Catalysis A: General, 530 (2017) 102-110.

[15] G. Zhu, J. Zhu, W. Jiang, Z. Zhang, J. Wang, Y. Zhu, Q. Zhang, Surface oxygen vacancy induced α-MnO$_2$ nanofiber for highly efficient ozone elimination, Applied Catalysis B: Environmental, 209 (2017) 729-737.

[16] J. Ma, C. Wang, H. He, Transition metal doped cryptomelane-type manganese oxide catalysts for ozone decomposition, Applied Catalysis B: Environmental, 201 (2017) 503-510.

[17] W. Hong, T. Zhu, Y. Sun, H. Wang, X. Li, F. Shen, Enhancing Oxygen Vacancies by Introducing Na(+) into OMS-2 Tunnels To Promote Catalytic Ozone Decomposition, Environmental science & technology, 53 (2019) 13332-13343.

[18] S. Gong, W. Li, Z. Xie, X. Ma, H. Liu, N. Han, Y. Chen, Low temperature decomposition of ozone by facilely synthesized cuprous oxide catalyst, New J. Chem., 41 (2017) 4828-4834.

[19] J. Jia, C. Qian, Y. Dong, Y.F. Li, H. Wang, M. Ghoussoub, K.T. Butler, A. Walsh, G.A. Ozin, Heterogeneous catalytic hydrogenation of CO$_2$ by metal oxides: defect engineering - perfecting imperfection, Chemical Society reviews, 46 (2017) 4631-4644.

[20] T. Xiong, Z.G. Yu, H. Wu, Y. Du, Q. Xie, J. Chen, Y.W. Zhang, S.J. Pennycook, W.S.V. Lee, J. Xue, Defect Engineering of Oxygen-Deficient Manganese Oxide to Achieve High-Performing Aqueous Zinc Ion Battery, Advanced Energy Materials, 9 (2019) 1803815.

[21] D.W. Kwon, G.J. Kim, J.M. Won, S.C. Hong, Influence of Mn valence state and characteristic of TiO$_2$ on the performance of Mn-Ti catalysts in ozone decomposition, Environ Technol, 38 (2017) 2785-2792.

[22] E. Rezaei, J. Soltan, N. Chen, Catalytic oxidation of toluene by ozone over alumina supported manganese oxides: Effect of catalyst loading, Applied Catalysis B: Environmental, 136-137 (2013) 239-247.

[23] Ebrahim Rezaei , Jafar Soltan , Ning Chen , J. Lin, Effect of noble metals on activity of MnOx-γ-alumina catalyst in catalytic ozonation of toluene, Chemical Engineering Journal, 214 (2013) 219-228.

[24] Rakesh Radhakrishnan, S.T. Oyama, Ozone Decomposition over Manganese Oxide Supported on ZrO$_2$ and TiO$_2$ A Kinetic Study Using in Situ Laser Raman Spectroscopy, Journal of Catalysis, 199 (2001) 182-290.

[25] Rakesh Radhakrishnan, S.T. Oyama, Electron Transfer Effects in Ozone Decomposition on Supported Manganese Oxide, Journal of Physical Chemisty.B, 105 (2001) 4245-4253.

[26] J. Jia, P. Zhang, L. Chen, The effect of morphology of α-MnO$_2$ on catalytic decomposition of gaseous ozone, Catal. Sci. Technol., 6 (2016) 5841-5847.

[27] J.D.P. H.J. Monkhorst, Special points for Brillouin-zone integrations, Physical Review B, 13 (1976) 5188-5192.

[28] T. Mishra , P. Mohapatra , K.M. Parida, Synthesis, characterisation and catalytic evaluation of iron–manganese mixed oxide pillared clay for VOC decomposition reaction, Applied Catalysis B: Environmental, 79 (2008) 279-285.

[29] A. Gil , M.A. Vicente , S.A. Korili, Effect of the nature and structure of pillared clays in the catalytic behaviour of supported manganese oxide, Catalysis Today, 112 (2006) 117-120.

[30] J. Chen, X. Chen, X. Chen, W. Xu, Z. Xu, H. Jia, J. Chen, Homogeneous introduction of CeO$_y$ into MnO$_x$ -based catalyst for oxidation of aromatic VOCs, Applied Catalysis B: Environmental, 224 (2018) 825-835.

[31] H. Sun, Z. Liu, S. Chen, X. Quan, The role of lattice oxygen on the activity and selectivity of the OMS-2 catalyst for the total oxidation of toluene, Chemical Engineering Journal, 270 (2015) 58-65.

[32] Y. Yang, J. Huang, S. Wang, S. Deng, B. Wang, G. Yu, Catalytic removal of gaseous unintentional POPs on manganese oxide octahedral molecular sieves, Applied Catalysis B: Environmental, 142-143 (2013) 568-578.

[33] D. Chen, D. He, J. Lu, L. Zhong, F. Liu, J. Liu, J. Yu, G. Wan, S. He, Y. Luo, Investigation of the role of surface lattice oxygen and bulk lattice oxygen migration of cerium-based oxygen carriers: XPS and designed H_2-TPR characterization, Applied Catalysis B: Environmental, 218 (2017) 249-259.

[34] J. Hou, L. Liu, Y. Li, M. Mao, H. Lv, X. Zhao, Tuning the K^+ concentration in the tunnel of OMS-2 nanorods leads to a significant enhancement of the catalytic activity for benzene oxidation, Environmental science & technology, 47 (2013) 13730-13736.

[35] C.H. Li Yang, Yulun Nie, Jiuhui Qu, Catalytic Ozonation of Selected Pharmaceuticals over Mesoporous Alumina-Supported Manganese Oxide, Environmental science & technology, 43 (2009) 2525-2529.

[36] J.P.D.A. John M. Roscoe, Diffuse Reflectance FTIR Study of the Interaction of Alumina Surfaces with Ozone and Water Vapor, The Journal of Physical Chemistry A, 109 (2005) 9028-9034.

[37] T. Gao, H. Fjellvag, P. Norby, A comparison study on Raman scattering properties of alpha- and beta-MnO_2, Analytica chimica acta, 648 (2009) 235-239.

[38] C. Julien, M. Massot, S. Rangan, M. Lemal, D. Guyomard, Study of structural defects in gama-MnO_2 by Raman spectroscopy, Journal of Raman Spectroscopy, 33 (2002) 223-228.

[39] C.M. Julien, M. Massot, C. Poinsignon, Lattice vibrations of manganese oxides, Spectrochimica Acta Part A: Molecular and Biomolecular Spectroscopy, 60 (2004) 689-700.

[40] E. Widjaja, J.T. Sampanthar, The detection of laser-induced structural change of MnO_2 using in situ Raman spectroscopy combined with self-modeling curve resolution technique, Analytica chimica acta, 585 (2007) 241-245.

Hosted file

`Figures.docx` available at https://authorea.com/users/319462/articles/449195-insights-into-the-roles-of-surface-oxygen-species-of-manganese-oxides-for-the-ozone-elimination-at-ambient-temperature